# Characterization of structural iron in smectites — an *ab initio* based XAS study

9 *Annamária Kéri[1,2,\*], Rainer Dähn[1], Matthias Krack[3], Sergey V. Churakov[1,2,\*]*

10 [1]Laboratory for Waste Management, Paul Scherrer Institute, CH-5232 Villigen PSI,
11 Switzerland

12 [2]Institute for Geological Sciences, University of Bern, CH-3012 Bern, Switzerland

13 [3]Laboratory for Scientific Computing and Modelling, Paul Scherrer Institute, CH-5232 Villigen
14 PSI, Switzerland

15 *Corresponding authors' e-mail: annamaria.keri@geo.unibe.ch; sergey.churakov@psi.ch

16                                Tel:  +41 56 310 4113

17                                Fax:  +41 56 310 2199

## Abstract

19 Fe-bearing clay minerals are abundant in argillaceous rocks as redox-active structural iron may
20 control the sorption mechanism of redox sensitive elements on the surface of clay minerals. The
21 extent and efficiency of the redox reactions depend on the oxidation state $\left(Fe^{2+}/Fe^{3+}\text{ ratio}\right)$ and
22 structural distribution of the substituting cations in the TOT-layer of clay minerals. Even
23 smectites with similar structure originating from different locations might have distinct
24 arrangement of isomorphic substitutions (e.g. individual iron or Fe–Fe pairs). In this study, the
25 proportion of different iron distribution in Milos–, Wyoming– and Texas–montmorillonite was
26 determined by combining X-ray absorption spectroscopy (XAS) with *ab initio* calculations. The
27 relaxed atomic structures of the smectite models with different arrangement of individual Fe
28 atoms and Fe–Fe/Fe–Mg clusters served as the basis for the calculations of the XAS spectra.
29 The combination of simulation results and measured Fe K-edge XAS spectra of Wyoming–,
30 Milos– and Texas–montmorillonites suggested that iron is present as $Fe^{3+}$ in the octahedral
31 sheet. $Fe^{3+}$ in Texas–montmorillonite has a tendency to form clusters, while no definitive
32 statement about clustering or avoidance of Fe–Fe and Fe–Mg pairs can be made for Milos– and
33 Wyoming–montmorillonite.

## 1. Introduction

Iron bearing clay minerals are one of the main redox controlling phases in soils[1]. They are important sorbents for organic and metallic contaminants as heterogeneous redox reactions on clay minerals control the mobility and bioavailability of redox-sensitive elements[2–5]. Understanding the mechanisms of individual redox reactions and the iron redox cycle is important in the interpretation of geochemical modelling[1,6]. However, redox processes are inherently complex phenomena and their detailed mechanism remained purely understood[5,6]. The behavior of the $Fe^{2+}/Fe^{3+}$ redox pairs has been studied in iron oxides (e.g. hematite[7,8], goethite[9,10]) and Fe-rich clay mineral (e.g. nontronite[4,11–14]), however, the redox processes in low Fe-bearing clay minerals (e.g. montmorillonite[3,15]) is much less understood[5]. A recent experimental study indicated that structural iron in Wyoming–montmorillonite is more accessible for an interfacial electron transfer than Texas–montmorillonite leading to the conclusion that low Fe-bearing clay minerals even with similar composition might have distinct arrangement of isomorphic substitutions[16].

The structure of Fe-bearing smectites can be described as layers of pseudo-hexagonally ordered sheets of alumina octahedral (O) sandwiched between two opposing siloxane tetrahedral (T) sheets (so called TOT-layer)[17,18]. Most of the Fe-bearing clay minerals belong to 2:1 type of dioctahedral smectites in which only two thirds of the possible octahedral positions are occupied[17]. One third of the octahedral sites are *trans*-symmetric and two thirds of the octahedral sites are *cis*-symmetric with respect to the orientation of the hydroxyl $(OH^-)$ groups[17,19]. It has been demonstrated that iron distribution in the octahedral and in the tetrahedral sheet strongly depends on the total Fe content[5,20–22]. Iron mainly substitutes for Al in the octahedral sheet where it can occupy both the *cis*- and the *trans*-sites[5,15,20,23,24]. It may have ordered distribution avoiding Fe–Fe or Fe–Mg pairing or it may form Fe–Fe and Fe–Mg edge sharing pairs of octahedra[15,19,20]. Clustering usually occurs in iron rich smectites (e.g. nontronite[2,11,25–27]), but it can also be observed in iron poor clay minerals[5,15]. The structure of the dioctahedral Fe-rich end-member, nontronite is well-studied and the relative distribution in the octahedral sheet of many cations $\left( e.g.\ Fe^{3+},\ Mg^{2+} \right)$ is quantified[5,12,13,28,29]. Much less is known about iron-poor smectites despite their importance in iron redox cycle of geochemical systems.

The redox-active structural iron in clay minerals with low Fe content may control the sorption mechanism and the oxidation state of redox sensitive elements on the clay mineral surface[5,15]. The uptake of ferrous iron on clays as well as the competitive sorption between $Fe^{2+}$ and other

67    divalent cations present in the system greatly depend on the concentration, the redox state and

68    the occupational site of structural iron[3,5,6,13,15,16,28,30,31]. The extent and efficiency of redox

69    reactions depends on the specific structural environment and oxidation state of cations in the

70    TOT-layer of clay minerals $\left( \text{e.g. } Fe^{2+}/Fe^{3+}, Mg^{2+} \right)$[5]. Due to electrostatic repulsion, $Fe^{3+}$

71    forming $Fe^{3+}$–$Fe^{2+}$ or $Fe^{3+}$–$Mg^{2+}$ clusters are less efficient electron acceptor in the redox

72    reaction[32]. In the best case, the phenomenon can be explained by the different structural

73    characteristics of the montmorillonites.

74    X-ray absorption spectroscopy (XAS) is a widely applied tool to identify the preferred oxidation

75    state and occupational site of iron in clay minerals[1,5,13,33]. For the quantitative interpretation,

76    reference spectra of minerals are needed, in which the element of interest has well-characterized

77    oxidation state. However, it is difficult to have material with pure $Fe^{2+}$ or $Fe^{3+}$ oxidation state

78    because iron preferentially participates in redox-reactions leading to materials with mixed

79    oxides[12,16,21]. Furthermore, iron can unequally be distributed between *cis-* and *trans-*octahedral

80    sites, which can barely or not at all be distinguished only by the experimental result of the

81    spectroscopic method[5,13,34]. Hence, it is becoming an increasingly widespread practice to

82    calculate the extended X-ray absorption fine structure (EXAFS) based on atomistic scale *ab*

83    *initio* simulations. The theoretical simulations of X-ray absorption near edge structure

84    (XANES) spectra for complex systems are still rare. Recent advances of the theory and

85    computational algorithms in the density functional theory with the local spin-density

86    approximation (DFT-LSDA) based model made it possible to obtain accurate Fe K-edge

87    XANES spectrum of a Fe-bearing structure[35,36].

88    In this work, we characterize the preferred oxidation state and distribution of iron in Milos−,

89    Wyoming− and Texas−montmorillonite by modelling the measured XAS spectra of these clay

90    minerals as a linear combination of theoretical spectra, which were obtained from *ab initio*

91    geometry optimization calculation of Fe-bearing smectites. The effect of Fe–Fe and Fe–Mg

92    clustering in the octahedral sheet on the XAS spectra was studied using several different

93    dioctahedral smectite models with structural iron incorporation in the octahedral sheet.

94　　**2. Materials and methods**

95　　**2.1. Modelling setup**

96　　In our study, we considered idealized defect free TOT layer of a 2:1 dioctahedral clay with the

97　　general formula of $4\cdot\left[\left(Mg_x Fe_y^{2+} Fe_z^{3+} Al_{8-x-y-z}\right)\left(Fe_n^{3+} Si_{16-n}\right)O_{40}(OH)_8\right]^{(x+y+n)-}$. It is often used

98　　as the simplest structural prototype for dioctahedral clays, where only two thirds of the cation

99　　sites in the octahedral sheet are occupied opening a possibility for two distinct structural

100　models[17]. In the *cis*-vacant model (*cv*-model), all *trans*-octahedra are occupied and half of the

101　*cis*- octahedra are vacant, while in the *trans*-vacant case (*tv*-model), all *trans*-octahedra are

102　vacant and all of the *cis*-octahedra are occupied (Figure 1)[37]. Natural clay minerals can be found

103　in both, *cis*- and *trans*-vacant forms[19,20,23].

104　In both models, the structural optimizations were performed on a single clay particle without

105　water in the interlayer. The dimensions of the orthorhombic supercell were

106　18.2Å×20.8Å×15.0Å. Similar to previous works, the cell parameter in the "*c*" direction was

107　fixed to 15Å to minimize the interaction between the periodic images[36–38].

108　The incorporation of iron in the structure was considered as a substitution for aluminum in the

109　octahedral sheet or for silicon in the tetrahedral sheet (Figure 1). Tetrahedral iron is evidently

110　always in the trivalent state, since $Fe^{2+}$ has a too large ionic radius for this site[5]. In the

111　octahedral sheet, both ferrous and ferric iron can occur. In the *tv*-model, iron is only present as

112　*cis*-octahedral positions whereas, in the *tv*-model Fe can be present in both (*cis*- or *trans*-)

113　octahedral positions (Figure 1). The effects of Fe–Fe clustering in the octahedral sheet was

114　studied by replacing two Al octahedra by a Fe–Fe pair at different occupational sites

115　(Figure 1d-g). The presence of Mg–Mg pairs as first and second neighbors produces

116　geometrical distortions in the octahedral sheet due to the higher radius of $Mg^{2+}$, furthermore,

117　the localized concentration of negative charge in the octahedral sheet would locally destabilize

118　the structure[39,40]. Similarly, the presence of $Fe^{2+}$–$Mg^{2+}$ pairs can be ruled out because of the

119　electrostatic repulsion argument. Thus, Fe–Mg clusters were modelled to $Fe^{3+}$–$Mg^{2+}$ pairs only

120　(Figure 1h-l). In total, 26 different model structures were evaluated (Figure 1, Table 1).
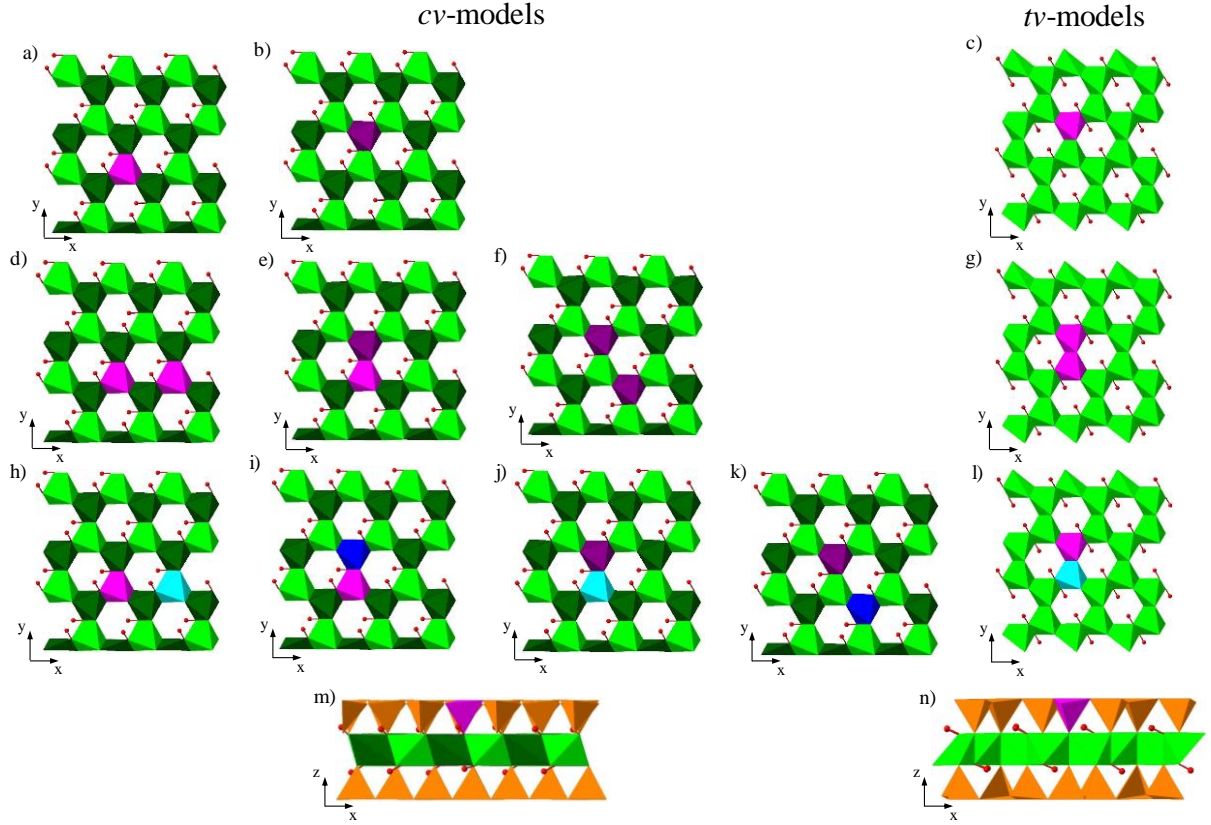
**Figure 1.** Schematic views of smectite models with different distribution of structural iron. Panel a-l indicate only the octahedral sheet for the sake of clarity. The structures with single iron atom per supercell corresponding to a random distribution are shown in panel a-c, configurations of Fe-Fe clusters are shown in panel d-g, while Mg-Fe clusters are shown in panel h-l. The distribution of tetrahedral iron is shown in panel m,n. *cv*-models correspond to panel a-b, d-f, h-k and m, while *tv*-models are shown in panel c, g, l and n. Silica tetrahedra are shown with orange color, while Fe, Mg and Al polyhedral (both octahedra and tetrahedra) are shown with pink, blue and green colors, respectively. *cis*-octahedra are represented with lighter, while *trans*-octahedra are marked with darker colors. The different occupational sites can be distinguished by the different relative position of the hydroxyl groups (OH⁻) shown with red spheres.

**Table 1.** Iron incorporation model, associated short name and panels of Figure 1 in which the corresponding model structure are. Illustrated relative energy differences are calculated for structures with the same stoichiometry and total charge.

| Tetrahedral/ octahedral Fe | Vacancy type | Oxidation state(s), occupational site(s) of iron(s)[a] | Short name of the model | Panel in Figure 1 | Cation[a]–Cation[a] bond length[b] [Å] | Energy difference[b] [kcal/mol] |
|---|---|---|---|---|---|---|
| Octahedral | $cv$ | $Fe^{2+}_{cis}$ | cvOctFe2c | a) | — | 0.0 ± 5.0 |
| | | $Fe^{2+}_{trans}$ | cvOctFe2t | b) | — | -4.2 ± 5.0 |
| | $tv$ | $Fe^{2+}_{cis}$ | tvOctFe2c | c) | — | -2.5 ± 5.0 |
| | $cv$ | $Fe^{3+}_{cis}$ | cvOctFe3c | a) | — | 0.0 ± 5.0 |
| | | $Fe^{3+}_{trans}$ | cvOctFe3t | b) | — | 0.3 ± 5.0 |
| | $tv$ | $Fe^{3+}_{cis}$ | tvOctFe3c | c) | — | -5.5 ± 5.0 |
| | $cv$ | $Fe^{2+}_{cis}$–$Fe^{2+}_{cis}$ | cvFe2cFe2c | d) | 5.20 ± 0.01 | 0.0 ± 5.0 |
| | | $Fe^{2+}_{cis}$–$Fe^{2+}_{trans}$ | cvFe2cFe2t | e) | 2.93 ± 0.01 | 6.3 ± 5.0 |
| | | $Fe^{2+}_{trans}$–$Fe^{2+}_{trans}$ | cvFe2tFe2t | f) | 5.27 ± 0.01 | -8.5 ± 5.0 |
| | $tv$ | $Fe^{2+}_{cis}$–$Fe^{2+}_{cis}$ | tvFe2cFe2c | g) | 3.01 ± 0.01 | 2.0 ± 5.0 |
| | $cv$ | $Fe^{2+}_{cis}$–$Fe^{3+}_{cis}$ | cvFe2cFe3c | d) | 5.20 ± 0.01 | 0.0 ± 5.0 |
| | | $Fe^{2+}_{cis}$–$Fe^{3+}_{trans}$ | cvFe2cFe3t | e) | 3.01 ± 0.01 | 0.7 ± 5.0 |
| | | $Fe^{2+}_{trans}$–$Fe^{3+}_{cis}$ | cvFe2tFe3c | e) | 3.05 ± 0.01 | -4.1 ± 5.0 |
| | | $Fe^{2+}_{trans}$–$Fe^{3+}_{trans}$ | cvFe2tFe3t | f) | 5.26 ± 0.01 | -3.7 ± 5.0 |
| | $tv$ | $Fe^{2+}_{cis}$–$Fe^{3+}_{cis}$ | tvFe2cFe3c | g) | 3.07 ± 0.01 | -5.8 ± 5.0 |
| | $cv$ | $Fe^{3+}_{cis}$–$Fe^{3+}_{cis}$ | cvFe3cFe3c | d) | 5.21 ± 0.01 | 0.0 ± 5.0 |
| | | $Fe^{3+}_{cis}$–$Fe^{3+}_{trans}$ | cvFe3cFe3t | e) | 3.07 ± 0.01 | 0.1 ± 5.0 |
| | | $Fe^{3+}_{trans}$–$Fe^{3+}_{trans}$ | cvFe3tFe3t | f) | 5.27 ± 0.01 | 0.1 ± 5.0 |
| | $tv$ | $Fe^{3+}_{cis}$–$Fe^{3+}_{cis}$ | tvFe3cFe3c | g) | 3.09 ± 0.01 | -6.4 ± 5.0 |
| | $cv$ | $Fe^{3+}_{cis}$–$Mg^{2+}_{cis}$ | cvMg2cFe3c | h) | 5.33 ± 0.01 | 0.0 ± 5.0 |
| | | $Fe^{3+}_{trans}$–$Mg^{2+}_{cis}$ | cvMg2cFe3t | i) | 3.11 ± 0.01 | -0.1 ± 5.0 |
| | | $Fe^{3+}_{cis}$–$Mg^{2+}_{trans}$ | cvMg2tFe3c | j) | 3.01 ± 0.01 | -1.9 ± 5.0 |
| | | $Fe^{3+}_{trans}$–$Mg^{2+}_{trans}$ | cvMg2tFe3t | k) | 5.24 ± 0.01 | -2.9 ± 5.0 |
| | $tv$ | $Fe^{3+}_{cis}$–$Mg^{2+}_{cis}$ | tvMg2cFe3c | l) | 3.00 ± 0.01 | -6.3 ± 5.0 |
| Tetrahedral | $cv$ | $Fe^{3+}$ | cvTetFe3 | m) | — | 0.0 ± 5.0 |
| | $tv$ | $Fe^{3+}$ | tvTetFe3 | n) | — | -7.3 ± 5.0 |

[a]Cation corresponds to $Fe^{2+}$, $Fe^{3+}$ or $Mg^{2+}$ depending on the structure

[b]More detailed information can be found in Table S1 in the Supporting Information 1

## 2.2. *Ab initio* calculations

The spin polarized electronic structures calculations were performed based on the density functional theory (DFT) using the Gaussian Plane Wave (GPW) method as it is implemented in the QUICKSTEP module of the CP2K code[41,42]. The scalar-relativistic norm-conserving pseudopotentials of Goedecker, Teter and Hutter (GTH)[43,44] were applied to avoid the explicit consideration of the core electrons. For iron, the core electrons were described as [Ne] and

142     $3s^2\ 3p^6\ 4s^2\ 3d^6$ were taken as valence electrons. The wave functions of valence electrons were

143     described by a linear combination of contracted Gaussian-type orbitals using MOLOPT basis

144     sets optimized for the corresponding GTH pseudopotentials[45]. An auxiliary basis set of plane

145     waves up to 400Ry cutoff energy was employed to expand the electronic density. The exchange

146     and correlation energy was calculated using the exchange-correlation functional of Perdew,

147     Burke and Ernzerhof (PBE)[46]. Simulations with single iron in the (tetrahedral or octahedral)

148     sheet were performed with a multiplicity $(2S+1)_{Fe^{2+}} = 5$ for systems with a single ferrous iron

149     and $(2S+1)_{Fe^{3+}} = 6$ for systems with a single ferric iron, respectively. For models representing

150     iron clustering with the same oxidation state, the multiplicity was set to

151     $(2S+1)_{Fe^{2+}-Fe^{2+}} = (2S+1)_{Fe^{3+}-Fe^{3+}} = 1$. For $Fe^{2+}$–$Fe^{3+}$ clusters, the multiplicity was set to

152     $(2S+1)_{Fe^{2+}-Fe^{3+}} = 2$.

153     Conventional DFT is known to underestimate the Coulomb repulsion between the localized $3d$-

154     electrons of Fe[47]. In order to improve the description of these delocalized states within the DFT

155     formalism, the so-called DFT+U method was applied[48,49]. In this semi empirical approach, an

156     additional potential characterized by the so-called Hubbard-parameter ($U_{eff}$) is applied to the

157     selected $3d$-states of Fe. The value of $U_{eff}$ depends on the implementation and has to be

158     calibrated[36]. The calibration for Fe-bearing montmorillonites was performed in our previous

159     paper[36], thus we used a fixed Hubbard-parameter with $U_{eff} = 1.9eV$ value.

160     **2.3. Calculations of EXAFS spectra**

161     The EXAFS spectra were calculated based on molecular configurations derived from *ab initio*

162     structure optimizations. Real space multiple scattering theory was applied as it is implemented

163     in the FEFF 8.40 software[50]. For each atomic configuration, the scattering potential of the atoms

164     were calculated self-consistently[50,51]. The amplitude reduction factor ($S_0^2$) was set to 1.0. Multi-

165     scattering paths up to eight legs with path lengths up to 7.0Å were taken into account. The

166     radius of the cluster for self-consistent full multiple scattering calculations was set to 5.0Å. A

167     Debye-Waller factor of $0.006Å^2$ was used to take into account the thermal and structural

168     disorder for the static configurations. Other parameters were kept to the default values[52]. All

169     calculated and measured spectra were normalized to the value of the first oscillation. The

170     calculated EXAFS spectra served as the basis for the interpretation of the experimental data.

171     The linear combination fit of the calculated to the experimental EXAFS spectra was performed

172     according to Eq.1 [36,37].

173
$$Q = \left(k^3 \sum_i \left(a_i^2 \chi_i(k)\right) - \chi^{\exp}(k)\right)^2 + \sum_i a_i^2 \to \min \qquad (1)$$

174 where $\chi_i(k)$ are the calculated and $\chi^{\exp}(k)$ is the experimental EXAFS spectra, $a_i^2$ are the

175 optimized fitting parameters. The fitting was limited to the interval of $k\left(\text{Å}^{-1}\right) \in [3.0, 9.0]$[36,37].

176 The norm $\sum_i a_i^2$ was included in the objective function to reduce the noise of the fit. The quality

177 of the fit is defined as Eq.1.[36,37]

## 2.4. XAS experiments

179 Four samples of low Fe-bearing montmorillonite samples were studied: one Milos− (Mil−),

180 one Wyoming-1− (SWy1−) and two Texas− (STx1$_1$−, STx1$_2$−) montmorillonite. All the samples

181 were prepared from the "as received" material without any physical or chemical treatment. Mil−

182 , SWy1− and STx1$_1$−samples were prepared as a self-supporting film, in addition, from the

183 Texas−montmorillonite, a sample was pressed into a pellet (STx1$_2$−sample). The Fe K-edge

184 XAS spectra were collected at the Stanford Synchrotron Radiation Lightsource (SSRL, Menlo

185 Park, CA) at beamline 11-2 using a Si(220) double crystal monochromator and a Canberra 100-

186 pixel Ge solid-state monolith detector. The self-supporting clay films were measured with

187 polarized extended X-ray absorption fine structure (P-EXAFS) spectroscopy at four different

188 angles ($\alpha$= 10°; 35°; 55°; 80°), where $\alpha$ is the angle between the electric field vector ($\varepsilon$) and

189 the layer plane of the self-supporting film. In P-EXAFS, neighboring atoms along the

190 polarization direction of the X-ray beam are preferentially probed, and atoms located in a plane

191 perpendicular to this direction are attenuated[53]. To test the potential texture effects arising from

192 the layered structures of the smectites, which tend to form samples having a certain degree of

193 texture[53,54], one STx1 sample was pressed as a pellet (STx1$_2$) and measured at $\alpha = 45°$. Several

194 scans were averaged to improve the signal to noise ratio. Higher order harmonics were rejected

195 by detuning the monochromator by 30%. The monochromator angle was calibrated at the Fe

196 K-edge by assigning the energy of 7112eV to the first inflection point of the K-edge absorption

197 spectrum of Fe metal foil.

198 All the P-EXAFS extraction from raw data (see details in Supporting Information 2) and all the

199 XAS data reduction was performed with the Athena/Artemis interface of IFEFFIT Software[55,56]

200 following standard procedures. The transformation from $\chi(E)$ to $\chi(k)$ were obtained by the

201 conversion of the abscissa using Eq.2.

202
$$k = \sqrt{\frac{2m_e}{\hbar^2}(E - E_0)} \qquad (2)$$

203 where $k$ is the wavelength, $m_e$ is the electron rest mass, $\hbar$ is the reduced Planck-constant and

204 $E_0$ is the edge energy. $E_0$ can automatically be determined by finding the first large peak of the

205 first derivative of the $\mu(E)$ spectrum in Athena[56], however, its value was usually

206 underestimated leading to a shift of the spectra in the $k$-space. Therefore, we applied an

207 alternative approach for our models. The EXAFS spectra of the models were quantitatively

208 compared to measured ones. To obtain the best linear combination fit for each measured sample,

209 their $\chi(E)$ spectrum was transformed to several $\chi(k)$ spectra using different $E_0$ around the

210 edge energy estimated by Athena. Afterwards, linear combination fits of each measured EXAFS

211 spectrum based on calculated ones were performed. The EXAFS quality numbers ($Q_{EXAFS}$)

212 from Eq.1 were calculated as the function of $E_0$ (Figure S2 in Supporting Information 2). We

213 accepted those fits for each montmorillonite type, which had the lowest $Q_{EXAFS}$ value.

214 **3. Results and Discussion**

215 **3.1. EXAFS spectra**

216 The calculated Fe K-edge EXAFS spectra for *cv*- and *tv*-model with ferric iron in the tetrahedral

217 sheet as well as $Fe^{2+}$ and $Fe^{3+}$ located in the *cis*- and *trans*- occupational sites in the octahedral

218 sheet are clearly distinct (Figure 2a)[36]. The first difference between the spectra with distinct

219 iron ionic state is a slight shift in the first oscillation at $k \sim 4.3/4.5 \text{Å}^{-1}$. A double-bounced

220 oscillation at $k \sim 6.1/6.6 \text{Å}^{-1}$ was present only for structures containing ferric iron[36]. Differences

221 could also be seen in the third oscillation ($k \sim 7.7/8.4 \text{Å}^{-1}$) where the shoulders are located at

222 the opposite side $\left(\text{left for } Fe^{2+} \text{ and right for } Fe^{3+}\right)$[36]. The calculated spectra for the tetrahedral

223 and the octahedral ferric iron clearly differ, as there is a $k \sim 0.5 \text{Å}^{-1}$ shift in the entire tetrahedral

224 ferric iron spectrum (Figure 2a,b). Iron in the *cis*- or *trans*-coordination (light and dark lines on

225 Figure 2a) turned out to have a minor effect on the obtained spectra. The result is consistent

226 with energy differences (Table 1).

227 Fourteen different EXAFS spectra representing structurally distinct Fe–Fe clusters for *cv*-

228 models were calculated (Figure 2c-e). In general, the spectra of $Fe^{2+}$–$Fe^{2+}$ clusters (Figure 2c)

229 were similar to the spectrum of a single $Fe^{2+}$ octahedron (individual $Fe^{2+}_{cis}$ or $Fe^{2+}_{trans}$ in the

230 octahedral sheet with short name "cvOctFe2c" and "cvOctFe2t" in Figure 2a). Similarly, the

231 spectra of $Fe^{3+}$–$Fe^{3+}$ clusters (Figure 2e) showed similarity to the spectrum of a single $Fe^{3+}$

232 octahedron (individual $Fe^{3+}_{cis}$ or $Fe^{3+}_{trans}$ in the octahedral sheet with short name "cvOctFe3c" and

233 "cvOctFe3t" in Figure 2a). The main sign of the similarity was the matching of the first peak

234 position ($k \sim 4.3 \pm 0.05 \text{Å}^{-1}$ for $Fe^{2+}$ and $k \sim 4.5 \pm 0.05 \text{Å}^{-1}$ for $Fe^{3+}$, respectively).
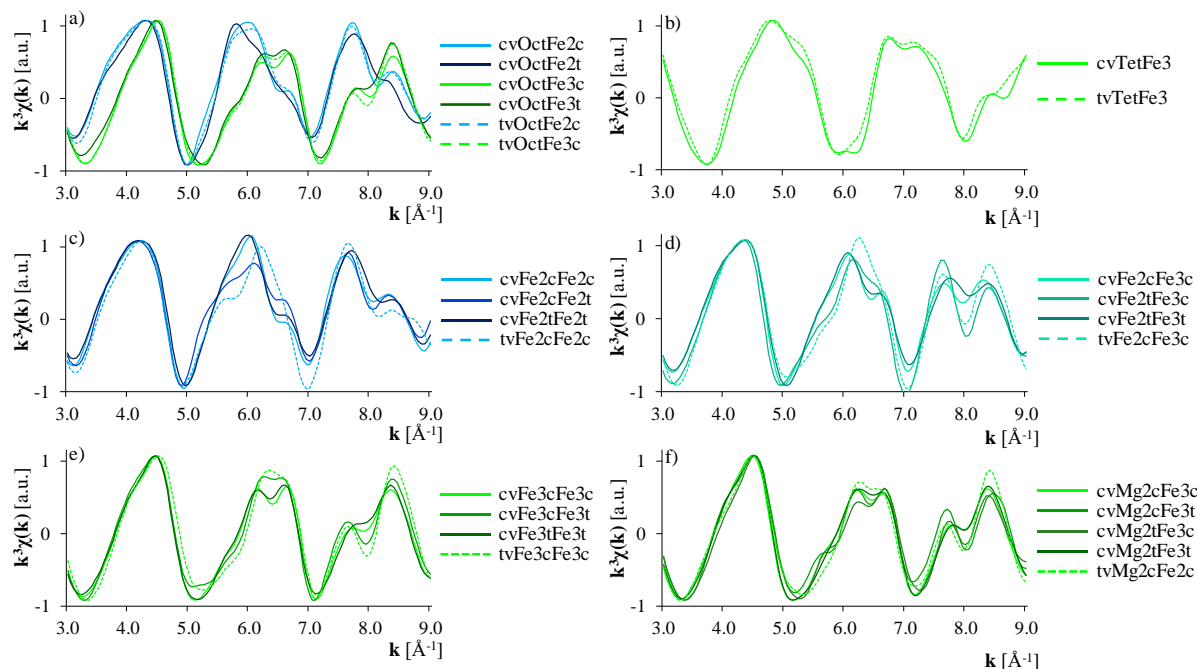


235

236 **Figure 2.** Modelled reference EXAFS spectra of Fe-bearing 2:1 clay minerals. In panel a and

237 b, EXAFS spectra of single iron incorporation in the octahedral[26] and tetrahedral sheet are

238 presented, respectively. Fe-Fe clusters are shown in panel c-e ($Fe^{2+}$-$Fe^{2+}$ in panel c, $Fe^{2+}$-$Fe^{3+}$

239 in panel d, $Fe^{3+}$-$Fe^{3+}$ in panel e), while $Mg^{2+}$-$Fe^{3+}$ clusters correspond to panel f. Blue color

240 represents $Fe^{2+}$, while $Fe^{3+}$ is marked with green color. Turquoise color in panel d represents

241 mixed ($Fe^{2+}$-$Fe^{3+}$) oxidation state. *Cis*-occupational sites are marked with lighter colors, darker

242 colors show *trans*-occupational sites, while mixed (*cis-trans* clusters) are represented with

243 medium bright colors, respectively. *cv*-model correspond to solid lines, while *tv*-model

244 represented by dashed lines. A more detailed explanation about the panels can be found in

245 Table 1.

246 Other features of the EXAFS spectra of the corresponding ionic state (right shoulder at the

247 second and the third oscillation for $Fe^{2+}$; double-bounced oscillation and left shoulder at the

248 third oscillation for $Fe^{3+}$) showed very good agreement for $Fe^{2+}_{cis}$–$Fe^{2+}_{cis}$ and $Fe^{2+}_{trans}$–$Fe^{2+}_{trans}$ as

249 well as $Fe^{3+}_{cis}$–$Fe^{3+}_{cis}$ and $Fe^{3+}_{trans}$–$Fe^{3+}_{trans}$ clustering models, respectively. Although, the shape and

250 the $k$ positions of the oscillations for the $Fe_{cis}$–$Fe_{trans}$ clustering models remained similar, the

251 second and the third oscillations altered. For the $Fe^{2+}$–$Fe^{2+}$ clusters (Figure 2c), the second

252 oscillation is lower and the right shoulder of it is more characteristic. In the case of $Fe^{3+}$–$Fe^{3+}$

253 clusters (Figure 2e), the double-bounced oscillation is more flattened and the left shoulder of

254   the third peak is higher. The spectra of $Fe^{2+}$–$Fe^{3+}$ (Figure 2d) did not correspond neither to

255   individual $Fe^{2+}$ ("cvOctFe2c" and "cvOctFe2t" in Figure 2a), nor to individual $Fe^{3+}$ spectra

256   ("cvOctFe3c" and "cvOctFe3t" in Figure 2a). The position of the first oscillation was at

257   $k \sim 4.4 \pm 0.05 Å^{-1}$, while for the second oscillation, it varied around $k \sim 6.2 \pm 0.1 Å^{-1}$ and for the

258   third, double-bounced oscillation the position was at $k \sim 7.70/8.5 Å^{-1}$ (Figure 2d). At the second

259   oscillation, a right shoulder was shown, for which intensity depended on the occupational sites

260   of the cluster. The EXAFS spectra of the *cv*-model with *cis-cis* and *trans-trans* occupational

261   site were similar, while differences in the intensity at the second and the third oscillation could

262   be observed for $Fe^{2+}_{trans}$–$Fe^{3+}_{cis}$ (Figure 2d). The differences can be explained by the Fe–O–Fe

263   scattering path (Table 1), which occurs only for clusters with different $Fe^{2+}_{cis}$–$Fe^{3+}_{trans}$ and $Fe^{2+}_{trans}$–

264   $Fe^{3+}_{cis}$ occupational sites (Figure 1e).

265   The four EXAFS spectra of the $Fe^{3+}$–$Mg^{2+}$ clusters for *cv*-model were very similar to the single

266   incorporated ferric iron one (Figure 2f). Only small differences in the high of the double-

267   bounced oscillation at $k \sim 6.30/6.65 Å^{-1}$ and of the third peak's shoulder at $k \sim 7.70 Å^{-1}$ could be

268   observed for $Fe^{3+}_{trans}$–$Mg^{2+}_{cis}$ and $Fe^{3+}_{cis}$–$Mg^{2+}_{trans}$ but not for $Fe^{3+}_{cis}$–$Mg^{2+}_{cis}$ and $Fe^{3+}_{trans}$–$Mg^{2+}_{trans}$. The

269   differences (similarly to Fe–Fe clustering) can be explained by the Fe–O–Mg scattering path

270   (Table S1 in Supporting Information 1), which occurs only for clusters with different

271   ($Fe^{3+}_{trans}$–$Mg^{2+}_{cis}$ and $Fe^{3+}_{cis}$–$Mg^{2+}_{trans}$) occupational sites (Figure 1i,j).

272   The corresponding EXAFS spectra of a single iron atom in the octahedral and tetrahedral

273   position of the *cv*- and *tv*-models agreed well (Figure 2a,b). The second and the third oscillation

274   of the spectra of Fe–Fe and Fe–Mg clusters in the *tv*-model have higher intensities than of the

275   corresponding $Fe_{cis}$–$Fe_{cis}$ and $Fe_{cis}$–$Mg_{cis}$ clusters of the *cv*-models, respectively. The EXAFS

276   spectra of Fe–Fe and Fe–Mg clusters in the *tv*-model show higher similarity to the *cv*-models

277   representing $Fe_{cis}$–$Fe_{trans}$, $Fe_{trans}$–$Fe_{cis}$ or $Fe_{trans}$–$Mg_{cis}$, $Fe_{cis}$–$Mg_{trans}$ models as Fe–O–Fe and

278   Fe–O–Mg scattering paths occur in the *tv*-models of these clusters. However, there are also

279   differences between the *cv*- and *tv*-model. The shoulder of the second oscillation for $Fe^{2+}$–$Fe^{2+}$

280   clusters appear at the left side of the oscillation, while the shape of the double-bound oscillation

281   for $Fe^{3+}$–$Fe^{3+}$ clusters is different. In addition, the shoulder at the second oscillation of the

282   $Fe^{2+}$–$Fe^{3+}$ cluster of the *tv*-model is lacking.

283 **3.2. Distribution of iron in low Fe-content montmorillonites**

284 The measured EXAFS spectra of the Milos– (Mil–), Wyoming– (SWy1–) and two Texas–

285 (STx1$_1$– and STx1$_2$–)montmorillonites were found to be rather similar. However, several

286 sample specific characteristic features can be seen at the second oscillation at $k \approx 6.1/6.6$ Å$^{-1}$

287 and in the intensity of the left shoulder of the third oscillation (Figure 3). The differences imply

288 distinct iron distribution in the bulk structure for Milos–, Wyoming– and Texas–

289 montmorillonites, while no differences between the two Texas–samples prepared as self-

290 supporting film and pellet (STx1$_1$– and STx1$_2$–) could be observed indicating that texture

291 effects in STx1$_2$–sample can be excluded.

292 The linear combination fits to the measured spectra for Mil–, SWy1–, STx1$_1$– and STx1$_2$–

293 montmorillonite using the theoretically calculated ones as basis were performed to obtain a

294 quantitative estimation of the preferential oxidation state and occupational sites of iron as well

295 as the preferred type of the clustering (single Fe tetrahedron and octahedron, Fe–Fe and Fe–Mg

296 clusters). *Cis–cis* and *trans–trans* occupational sites in the *cv*-vacant smectite models

297 (Figure 1d,f,h,k) were considered to be structurally equivalent to individual Fe in the octahedral

298 sheet because the two metal (Fe–Fe or Fe–Mg) ion did not influence each other valence orbital

299 (Table S1 in Supporting Information 1). Thus, for Fe–Fe and Fe–Mg clusters in the *cv*-model,

300 only *cis–trans* and *trans–cis* clusters were explicitly considered (Figure 1e,i,j). In the *tv*-model,

301 Fe–Fe and Fe–Mg substitutions were considered as near neighbor clusters.

302 The best EXAFS linear combination fits (Figure 3a,c,e,f) indicated that iron is present almost

303 exclusively in the Fe$^{3+}$ form in all montmorillonite type ("Fit1" in Table 2). This result agreed

304 well with the assumption of earlier studies[22,36]. The differences among the samples appeared in

305 the distribution of iron. The results of linear combination fit suggested that iron has ordered

306 distribution in Wyoming–montmorillonite, while in Milos– and Texas–montmorillonites

307 6–18% of iron takes part in Fe–Fe clusters ("Fit1" in Table 2). Fe–Mg clusters could provide

308 up to 9–12% contribution in Texas–montmorillonites. Octahedral iron is equally distributed

309 between the occupational sites in Wyoming– and Texas–samples, *trans*-site preference

310 occurred only in Milos–montmorillonite ("Fit1" in Table 2). The energy comparison of the

311 *cis*/*trans*-models with similar isomorphic substitutions and iron oxidation states indicated that

312 there is no site preference in bulk smectites (Table 1).
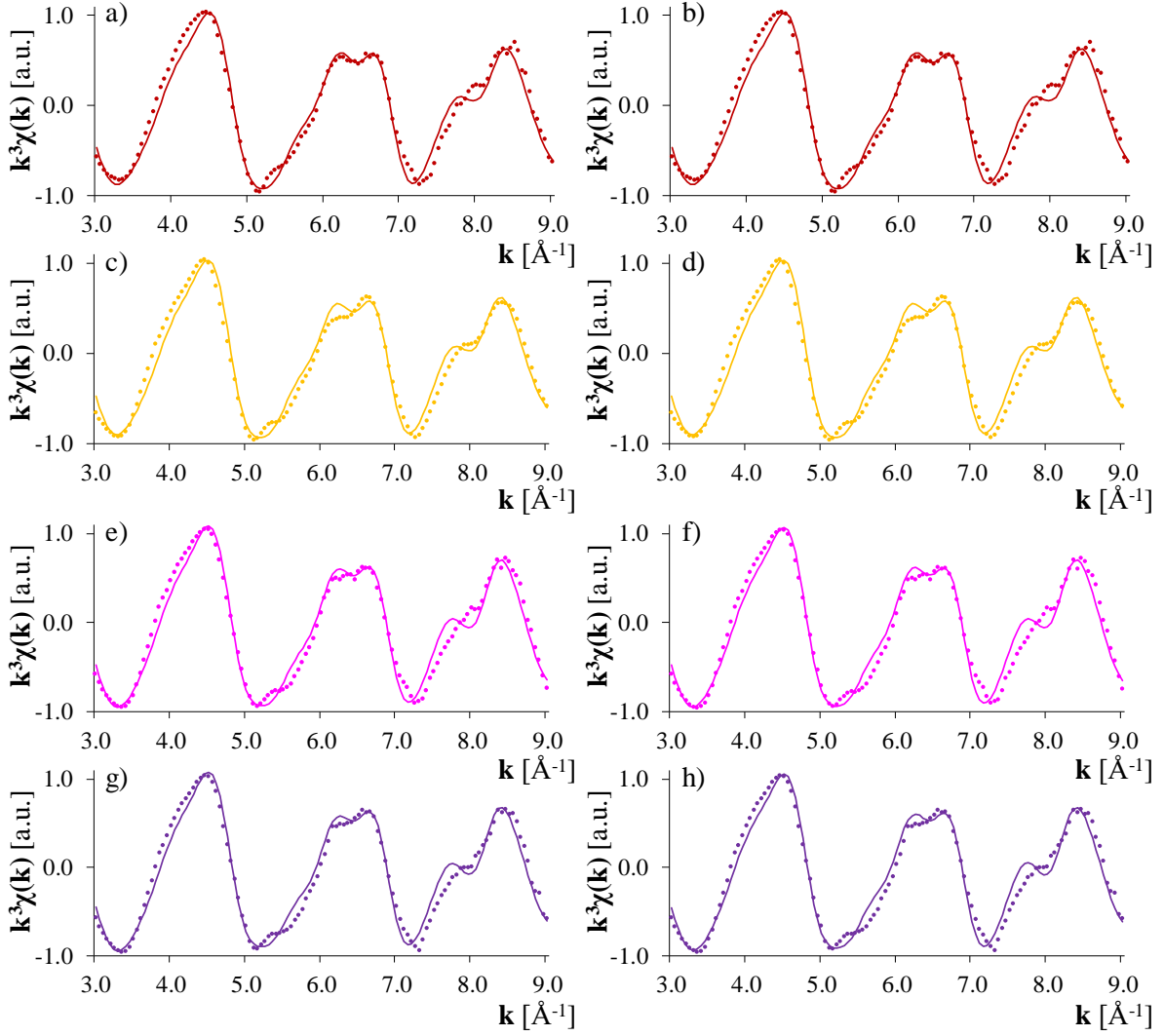
313

**Figure 3.** Experimental EXAFS spectra (dots) with the corresponding best linear combination fits (solid lines) based on the contributions shown in Table 2. In panel a, red color corresponds to Mil-montmorillonite, orange color represents SWy-montmorillonite in panel b, while pink and purple colors show STx$_1$- and STx$_2$-montmorillonites in panel c and d, respectively.

**Table 2.** Parameters (contributions [%] and quality [–]) of the EXAFS linear combination fit of distinct smectite models for Mil–, SWy1–, STx1$_1$– and STx1$_2$–montmorillonite

| Smectite model name[a] | Mil [%] | | | | SWy1 [%] | | | | STx1$_1$ [%] | | | | STx1$_2$ [%] | | | |
|---|---|---|---|---|---|---|---|---|---|---|---|---|---|---|---|---|
| Fit number[b] | Fit1 | Fit2 | Fit3 | Fit4 | Fit1 | Fit2 | Fit3 | Fit4 | Fit1 | Fit2 | Fit3 | Fit4 | Fit1 | Fit2 | Fit3 | Fit4 |
| cvOctFe2c | <1 | <1 | <1 | 1 | <1 | <1 | <1 | <1 | <1 | <1 | <1 | <1 | <1 | <1 | <1 | <1 |
| cvOctFe2t | <1 | <1 | <1 | <1 | <1 | <1 | <1 | <1 | <1 | <1 | <1 | <1 | <1 | <1 | <1 | <1 |
| tvOctFe2c | <1 | <1 | <1 | <1 | <1 | <1 | <1 | <1 | <1 | <1 | <1 | <1 | <1 | <1 | <1 | <1 |
| cvOctFe3c | <1 | <1 | 7 | 8 | 16 | 16 | 23 | 21 | 4 | 5 | 10 | 10 | 8 | 7 | 13 | 13 |
| cvOctFe3t | 20 | 20 | 24 | 31 | 14 | 14 | 24 | 20 | 8 | 6 | 12 | 17 | 6 | 3 | 10 | 15 |
| tvOctFe3c | 3 | 3 | 8 | 10 | 4 | 4 | 9 | 9 | 7 | 8 | 14 | 15 | 6 | 7 | 12 | 15 |
| [d]cvFe2cFe2c | <1 | <1 | <1 | — | <1 | <1 | <1 | — | <1 | <1 | <1 | — | <1 | <1 | <1 | — |
| [d]cvFe2cFe2t | <1 | <1 | <1 | — | <1 | <1 | <1 | — | <1 | <1 | <1 | — | <1 | <1 | <1 | — |
| [d]cvFe2tFe2t | <1 | <1 | <1 | — | <1 | <1 | <1 | — | <1 | <1 | <1 | — | <1 | <1 | <1 | — |
| [d]tvFe2cFe2c | <1 | <1 | <1 | — | <1 | <1 | <1 | — | <1 | <1 | <1 | — | <1 | <1 | <1 | — |
| [d]cvFe2cFe3c | <1 | <1 | <1 | — | <1 | <1 | <1 | — | <1 | <1 | <1 | — | <1 | <1 | <1 | — |
| [d,e]cvFe2cFe3t | — | — | — | — | — | — | — | — | — | — | — | — | — | — | — | — |
| [d]cvFe2tFe3c | <1 | <1 | <1 | — | <1 | <1 | <1 | — | <1 | <1 | <1 | — | <1 | <1 | <1 | — |
| [d]cvFe2tFe3t | 6 | 6 | 8 | — | <1 | <1 | <1 | — | <1 | <1 | <1 | — | <1 | <1 | <1 | — |
| [d]tvFe2cFe3c | <1 | <1 | <1 | — | <1 | <1 | <1 | — | <1 | <1 | <1 | — | <1 | <1 | <1 | — |
| [d]cvFe3cFe3c | 10 | 10 | 14 | — | 7 | 7 | 13 | — | 11 | 12 | 16 | — | 9 | 10 | 13 | — |
| [d]cvFe3cFe3t | 2 | 2 | 4 | — | 1 | 1 | 4 | — | 1 | 2 | <1 | — | 8 | 10 | 11 | — |
| [d]cvFe3tFe3t | 27 | 27 | 32 | — | 22 | 22 | 29 | — | 23 | 23 | 30 | — | 19 | 18 | 24 | — |
| [d]tvFe3cFe3c | 3 | 3 | 4 | — | <1 | <1 | <1 | — | 10 | 12 | 16 | — | 9 | 13 | 14 | — |
| [d]cvMg2cFe3c | 7 | 7 | — | 16 | 13 | 13 | — | 18 | <1 | <1 | — | 6 | 2 | <1 | — | 7 |
| [d]cvMg2cFe3t | <1 | <1 | — | <1 | <1 | <1 | — | <1 | <1 | <1 | — | <1 | 1 | 7 | — | <1 |
| [d]cvMg2tFe3c | <1 | <1 | — | <1 | <1 | <1 | — | <1 | <1 | <1 | — | <1 | <1 | <1 | — | <1 |
| [d]cvMg2tFe3t | 19 | 19 | — | 29 | 22 | 22 | — | 28 | 21 | 20 | — | 29 | 20 | 18 | — | 28 |
| [d]tvMg2cFe3c | <1 | <1 | — | 5 | 1 | 1 | — | 3 | 12 | 12 | — | 21 | 8 | 7 | — | 18 |
| cvTetFe3 | <1 | — | <1 | <1 | <1 | — | <1 | <1 | <1 | — | 1 | <1 | 1 | — | 3 | <1 |
| tvTetFe3 | <1 | — | <1 | <1 | <1 | — | <1 | <1 | 2 | — | <1 | 3 | 2 | — | <1 | 5 |
| [b]∑ Fe$^{2+}$ | **3** | **3** | **4** | **1** | **<1** | **<1** | **<1** | **<1** | **<1** | **<1** | **<1** | **<1** | **<1** | **<1** | **<1** | **<1** |
| [b]∑ Fe$^{3+}$ | **97** | **97** | **96** | **99** | **100** | **100** | **100** | **100** | **100** | **100** | **100** | **100** | **100** | **100** | **100** | **100** |
| [c]∑ Fe$_{ordered\ tetrahedron}$ | **<1** | **—** | **<1** | **<1** | **<1** | **—** | **<1** | **<1** | **2** | **—** | **1** | **3** | **3** | **—** | **3** | **5** |
| [c]∑ Fe$_{ordered\ octahedron}$ | **94** | **94** | **92** | **95** | **97** | **97** | **96** | **97** | **75** | **74** | **82** | **77** | **70** | **63** | **73** | **77** |
| [c,d]∑ Fe–Fe cluster | **6** | **6** | **8** | **—** | **2** | **2** | **4** | **—** | **11** | **14** | **17** | **—** | **18** | **22** | **24** | **—** |
| [c,d]∑ Mg–Fe cluster | **<1** | **<1** | **—** | **5** | **1** | **1** | **—** | **3** | **12** | **12** | **—** | **21** | **9** | **15** | **—** | **18** |
| [c]∑ Fe$_{cis}$ | 26 | 26 | 35 | 40 | 42 | 42 | 45 | 51 | 46 | 50 | 43 | 51 | 47 | 49 | 58 | 53 |
| [c]∑ Fe$_{trans}$ | 74 | 74 | 65 | 60 | 58 | 58 | 55 | 49 | 52 | 50 | 56 | 46 | 50 | 51 | 39 | 43 |
| Q [–] | 2.36 | 2.36 | 2.40 | 2.49 | 2.39 | 2.39 | 2.46 | 2.43 | 2.68 | 2.68 | 2.76 | 2.80 | 2.57 | 2.58 | 2.62 | 2.67 |

[a]Short name of the smectite models are explained in Table 1

[b]"Fit1" corresponds to "best fit", while "Fit2", "Fit3" and "Fit4" are constrained models without tetrahedral iron, Fe–Mg and Fe–Fe pairs, respectively

[c]The results were derived from the raw data written in the first "section" of the table

[d]Only *trans*-vacant (*tv*) and Fe$_{cis}$–Fe$_{trans}$, Fe$_{trans}$–Fe$_{cis}$, Fe$_{trans}$–Mg$_{cis}$ and Fe$_{cis}$–Mg$_{trans}$ from *cis*-vacant (*cv*) structures were considered as Fe–Fe and Fe–Mg clusters, respectively

[e]The spectra of this model was not included in the fit due to fatal error of FEFF run

320 No tetrahedral iron can be found in Milos− or in Wyoming−montmorillonite ("Fit1" in Table 2),

321 furthermore, in $STx1_1$− and $STx1_2$−montmorillonite samples, the very low amount ~1–2% of

322 tetrahedral iron is below the estimated absolute uncertainty $(\pm15\%)$[37] for the linear combination

323 fit ("Fit1" in Table 2). The results suggested that tetrahedral iron is negligible. To estimate the

324 importance of tetrahedral iron for the fit quality, another fit ("Fit2") with only octahedral iron

325 substitution models was performed for the measured EXAFS data sets. The results indicate that

326 the exclusion of the tetrahedral iron has negligible effect on the fits of Milos− and Wyoming−

327 montmorillonites as their "Fit2" EXAFS spectra (Figure 3a-d) and the corresponding fitting

328 parameters (contribution and quality number) were identical (Table 2) to the previous best fits

329 ("Fit1"). Similar conclusion could be made for Texas−montmorillonite samples as tetrahedral

330 iron models barely influence the shape of the EXAFS spectra (little increment in the left

331 shoulder of the second oscillation) while the quality numbers agree with the best fit results

332 within the uncertainty. The contribution of Fe–Fe and Fe–Mg clustering models in "Fit2" is

333 increased, while small reduction of the individual Fe in the octahedral sheet is observed.

334 Sensitivity analysis for Fe–Fe and Fe–Mg clustering were determined performing "Fit3" and

335 "Fit4" without Fe–Fe and Fe–Mg pairs, respectively. The quality number of the fits show that

336 the exclusion of Fe–Fe or Fe–Mg pairs from the fitting data set of reference spectra reduces the

337 quality of the fit. In such a constraint fit, the contribution of the excluded clusters are

338 redistributed among the remaining components of the fit. The omission of Fe–Fe pairs has

339 larger effect on Milos− and Texas−samples, while the omission of Fe–Mg pairs shows more

340 significant impact for the Wyoming-sample.

341 Conventional ("shell-by-shell") P-EXAFS fits were also performed on the Mil−, SWy1− and

342 $STx1_1$−samples (Supporting Information 2). The results revealed that quite a few constrains

343 obtained from *ab initio* calculations (e.g. coordination number of Al, Fe and first O shell, co-

344 varying $CN_{Fe-O/Al/Fe/Si}(\alpha)$ and $\alpha$ through a polarization parameter are necessary to reduce the

345 number of independent fitting parameters (Supporting Information 2)[57,58]. The conventional P-

346 EXAFS fitting results (Table S1 in Supporting Information 2) agree well with the interatomic

347 distances and coordination numbers of relax structures containing $Fe^{3+}$ (Table S1 in

348 Supporting Information 1). However, the differences present in the P-EXAFS spectra of the

349 three montmorillonite cannot be explained by using the "shell-by-shell" fit approach alone.

350 The XANES spectra of the different smectite models were also calculated and compared to the

351 measured Milos−, Wyoming− and Texas−montmorillonites (Supporting Information 2). The

352 results show that tetrahedral iron models have very different XANES spectra compared to the

353  four measured spectra (Figure S3,S4 in Supporting Information 2). The measurement results

354  agree well with the calculated XANES spectra containing only octahedral ferric iron

355  (Figure S3,S4 in Supporting Information 2). However, XANES spectra turned out to be very

356  similar for all (Figure S3 in Supporting Information 2).


357  **4. Implication of the structural position of Fe in bulk montmorillonite**


358  This study reveals structural differences in Fe -bearing Milos–, Wyoming– and Texas–

359  montmorillonites. The very distinct EXAFS and XANES spectra of tetrahedral iron indicate

360  that there is no significant amount of tetrahedral iron in low Fe-bearing smectites. Potential

361  presence of tetrahedral iron suggested in earlier studies[5,59] cannot be confirmed on the basis of

362  studied data.

363  The proportion of Fe–Fe and Fe–Mg clustering in different montmorillonite samples needs

364  separate discussion. Depending on the total number of Fe and Mg substitutions in the sample,

365  there is a finite probability of clusters to form in case of random (e.g. no energetically preferred

366  interaction) distribution of Mg and Fe sites. The positive or negative deviation of EXAFS

367  fitting results from the expectation value for a random distribution of sites will indicate an

368  energy driven preferential cluster formation or avoidance, respectively. The probability of

369  randomly formed cluster was evaluated by Monte Carlo simulation for the given composition

370  of in SWy1–, STx1– and Mil–montmorillonite (Supporting Information 1). Number of Fe–Mg

371  and Fe–Fe clusters estimated for STx1–montmorillonite from the EXAFS fit is significantly

372  larger than the expected value for a random distribution. This result is consistent with data

373  reported by Vantelon et al.[22] and the estimation of lattice energy for cluster formation (Table S2

374  in Supporting Information 1). For the Mil– and SWy1–montmorillonite, the number of clusters

375  predicted by EXAFS is comparable with the random distribution. Taking into account the

376  modelling uncertainties and intrinsically low amount of Fe and Mg substitutions, no definitive

377  statement about possible slight clustering or avoidance of Fe–Fe and Fe–Mg pair can be made

378  for Mil– and SWy1–montmorillonite based on the fitting results.

379  The differences in the iron distribution explain the varying Fe uptake behavior of these

380  montmorillonites. Due to the electrostatic repulsion, ferric iron present in $Fe^{3+}$–$Mg^{2+}$ clusters

381  is a less efficient electron acceptor in the redox reaction than in $Fe^{3+}$–$Fe^{3+}$ clusters or individual

382  $Fe^{3+}$ in the octahedral sheet. $Fe^{3+}$–$Mg^{2+}$ clusters could be present in Texas–samples but not in

383  Wyoming–montmorillonite[32]. This would explain the higher redox capacity of SWy1–

384 montmorillonite derived from a wet chemistry and XAS spectroscopy measurement[16]. There

385 might be certain electron small polaron hopping conduction pathways, which assist the

386 oxidative sorption of iron $\left(Fe_{aq}^{2+} \rightarrow Fe_{surf}^{3+}\right)$. Therefore, in addition to the surface specifications

387 (e.g. surface site, protonation scheme, inner-/outer-sphere complex), the effect of cation

388 substitution in the bulk structure should also be studied.

389 Our investigations had to deal with the challenge of XAS measurements of low iron amount.

390 Although the linear combination fit of the calculated spectra showed very good agreement with

391 Milos−montmorillonite sample, the fit had lower quality for Wyoming− and Texas−

392 montmorillonites. Potential explanation could be the presence of $Al^{3+}$ substitution in the

393 tetrahedral sheet, which were not considered in this study but have an impact on the bulk

394 structure.

408 **Supporting Information**

409 Supporting Information 1: Details on theoretical studies

410 Supporting Information 2: Details on P-EXAFS data analysis and XANES calculations

411 **References**

412 (1)  Stucki, J. W.; Goodman, B. A.; Schwertamann, U. *Iron in Soils and Clay Minerals*.

413       Dordrecht, Netherlands, **2012**, pp. 1–3.

(2)   Ilgen, A. G.; Kukkadapu, R. K.; Dunphy, D. R.; Artyushkova, K.; Cerrato, J. M.; Kruichak, J. N.; Janish, M. T.; Sun, C. J.; Argo, J. M.; Washington, R. E. Synthesis and Characterization of Redox-Active Ferric Nontronite. *Chem. Geol.* **2017**, *470*, 1–12.

(3)   Soltermann, D.; Marques Fernandes, M.; Baeyens, B.; Miehé-Brendlé, J.; Dähn, R. Competitive Fe(II)–Zn(II) Uptake on a Synthetic Montmorillonite. *Environ. Sci. Technol.* **2013**, *48(1)*, 190–198.

(4)   Hofstetter, T. B.; Schwarzenbach, R. P.; Haderlein, S. B. Reactivity of Fe(II) Species Associated with Clay Minerals. *Environ. Sci. Technol.* **2003**, *37(3)*, 519–528.

(5)   Stucki, J. W. Properties and Behaviour of Iron in Clay Minerals. In *Handbook of Clay Science*; **2006**, *Vol. 1*, pp. 423–475.

(6)   Stucki, J. W. A Review of the Effects of Iron Redox Cycles on Smectite Properties. *Comptes Rendus Geosci.* **2011**, *343*, 199–209.

(7)   Kerisit, S.; Rosso, K. M. Computer Simulation of Electron Transfer at Hematite Surfaces. *Geochim. Cosmochim. Acta* **2006**, *70(8)*, 1888–1903.

(8)   Williams, A. G. B.; Scherer, M. M. Spectroscopic Evidence for Fe(II)–Fe(III) Electron Transfer at the Iron Oxide−Water Interface. *Environ. Sci. Technol.* **2004**, *38(18)*, 4782–4790.

(9)   Alexandrov, V.; Rosso, K. M. Insights into the Mechanism of Fe(II) Adsorption and Oxidation at Fe–Clay Mineral Surfaces from First-Principles Calculations. *J. Phys. Chem. C* **2013**, *117(44)*, 22880–22886.

(10)  Zarzycki, P.; Kerisit, S.; Rosso, K. M. Molecular Dynamics Study of Fe(II) Adsorption, Electron Exchange, and Mobility at Goethite (α–FeOOH) Surfaces. *J. Phys. Chem. C* **2015**, *119(6)*, 3111–3123.

(11)  Gorski, C. A.; Aeschbacher, M.; Soltermann, D.; Voegelin, A.; Baeyens, B.; Marques Fernandes, M.; Hofstetter, T. B.; Sander, M. Redox Properties of Structural Fe in Clay Minerals. 1. Electrochemical Quantification of Electron-Donating and -Accepting Capacities of Smectites. *Environ. Sci. Technol.* **2012**, *46(17)*, 9360–9368.

(12)  Manceau, A.; Lanson, B.; Drits, V. A.; Chateigner, D.; Gates, W. P.; Wu, J.; Huo, D.; Stucki, J. W. Oxidation-Reduction Mechanism of Iron in Dioctahedral Smectites: I. Crystal Chemistry of Oxidized Reference Nontronites. *Am. Mineral.* **2000**, *85(1)*, 133–152.

445  (13)  Manceau, A.; Drits, V. A.; Lanson, B.; Chateigner, D.; Wu, J.; Huo, D.; Gates, W. P.;
446        Stucki, J. W. Oxidation-Reduction Mechanism of Iron in Dioctahedral Smectites: II.
447        Crystal Chemistry of Reduced Garfield Nontronite. *Am. Mineral.* **2000**, *85(1)*, 153–172.

448  (14)  Hofstetter, T. B.; Neumann, A.; Schwarzenbach, R. P. Reduction of Nitroaromatic
449        Compounds by Fe(II) Species Associated with Iron-Rich Smectites. *Environ. Sci.*
450        *Technol.* **2006**, *40(1)*, 235–242.

451  (15)  Neumann, A.; Sander, M.; Hofstetter, T. B. *Redox Properties of Structural Fe in*
452        *Smectite Clay Minerals*. **2011**, pp. 361–379.

453  (16)  Soltermann, D.; Marques Fernandes, M.; Baeyens, B.; Dähn, R.; Joshi, P. A.; Scheinost,
454        A. C.; Gorski, C. A. Fe(II) Uptake on Natural Montmorillonites. I. Macroscopic and
455        Spectroscopic Characterization. *Environ. Sci. Technol.* **2014**, *48(15)*, 8688–8697.

456  (17)  Guggenheim, S.; Adams, J. M.; Bain, D. C.; Bergaya, F.; Brigatti, M. F.; Drits, V. A.;
457        Formosso, M. L. L.; Galan, E.; Kogure, T.; Stanjek, H. Summary of Recommendations
458        of Nomenclature Committees Relevant to Clay Mineralogy: Report of the Association
459        Internationale Pour l'Etude Des Argiles (AIPEA) Nomenclature Committee for 2006.
460        *Clays Clay Miner.* **2006**, *54(6)*, 761–772.

461  (18)  Stucki, J. W.; Lee, K.; Zhang, L.; Larson, R. A. Effects of Iron Oxidation State on the
462        Surface and Structural Properties of Smectites. *Pure Appl. Chem.* **2002**, *74(11)*, 2081–
463        2094.

464  (19)  Drits, V. A.; McCarty, D. K.; Zviagina, B. B. Crystal-Chemical Factors Responsible for
465        the Distribution of Octahedral Cations over *Trans*- and *Cis*-Sites in Dioctahedral 2:1
466        Layer Silicates. *Clays Clay Miner.* **2006**, *54(2)*, 131–152.

467  (20)  Wolters, F.; Lagaly, G.; Kahr, G.; Nueesch, R.; Emmerich, K. A Comprehensive
468        Characterization of Dioctahedral Smectites. *Clays Clay Miner.* **2009**, *57(1)*, 115–133.

469  (21)  Gates, W. P.; Slade, P. G.; Manceau, A.; Lanson, B. Site Occupancies by Iron in
470        Nontronites. *Clays Clay Miner.* **2002**, *50(2)*, 223–239.

471  (22)  Vantelon, D.; Montarges-Pelletier, E.; Michot, L. J.; Pelletier, M.; Thomas, F.; Briois,
472        V. Iron Distribution in the Octahedral Sheet of Dioctahedral Smectites. An Fe K-Edge
473        X-Ray Absorption Spectroscopy Study. *Phys. Chem. Miner.* **2003**, *30(1)*, 44–53.

474    (23)    Tsipursky, S. I.; Drits, V. A. The Distribution of Octahedral Cations in the 2:1 Layers of
475            Dioctahedral Smectites Studied by Oblique-Texture Electron Diffraction. *Clay Miner.*
476            **1984**, *19(2)*, 177–193.

477    (24)    Vantelon, D.; Pelletier, M.; Michot, L. J.; Barres, O.; Thomas, F. Fe, Mg and Al
478            Distribution in the Octhaedral Sheet of Montmorillonites. An Infrared Study in the $OH^-$
479            Bending Region. *Clay Miner.* **2001**, *36*, 360–379.

480    (25)    Gorski, C. A.; Klüpfel, L.; Voegelin, A.; Sander, M.; Hofstetter, T. B. Redox Properties
481            of Structural Fe in Clay Minerals. 2. Electrochemical and Spectroscopic
482            Characterization of Electron Transfer Irreversibility in Ferruginous Smectite, SWa-1.
483            *Environ. Sci. Technol.* **2012**, *46(17)*, 9369–9377.

484    (26)    Gorski, C. A.; Klüpfel, L. E.; Voegelin, A.; Sander, M.; Hofstetter, T. B. Redox
485            Properties of Structural Fe in Clay Minerals: 3. Relationships between Smectite Redox
486            and Structural Properties. *Environ. Sci. Technol.* **2013**, *47(23)*, 13477–13485.

487    (27)    Cashion, J. D.; Gates, W. P.; Riley, G. M. Origin of the Two Quadrupole Doublets in
488            NAu-1 Nontronite. *J. Phys. Conf. Ser.* **2010**, *217(1)*, 012065.

489    (28)    Stucki, J. W.; Golden, D. C.; Roth, C. B. Effects of Reduction and Reoxidation of
490            Structural Iron on the Surface Charge and Dissolution of Dioctahedral Smectites. *Clays*
491            *Clay Miner.* **1984**, *32(5)*, 350–356.

492    (29)    Fialips, C.-I.; Huo, D.; Yan, L.; Wu, J.; Stucki, J. W. Effect of Fe Oxidation State on the
493            IR Spectra of Garfield Nontronite. *Am. Mineral.* **2002**, *87(5–6)*, 630–641.

494    (30)    Soltermann, D.; Baeyens, B.; Bradbury, M. H.; Marques Fernandes, M. Fe(II) Uptake
495            on Natural Montmorillonites. II. Surface Complexation Modeling. *Environ. Sci. Technol.*
496            **2014**, *48(15)*, 8698–8705.

497    (31)    Neumann, A.; Petit, S.; Hofstetter, T. B. Evaluation of Redox-Active Iron Sites in
498            Smectites Using Middle and near Infrared Spectroscopy. *Geochim. Cosmochim. Acta*
499            **2011**, *75(9)*, 2336–2355.

500    (32)    Rosso, K. M.; Ilton, E. S. Effects of Compositional Defects on Small Polaron Hopping
501            in Micas. *J. Chem. Phys.* **2005**, *122(24)*, 244709.

502    (33)    Finck, N.; Schlegel, M. L.; Dardenne, K.; Adam, C.; Kraft, S.; Bauer, A.; Robert, J.-L.
503            Structural Iron in Smectites with Different Charge Locations. *Phys. Chem. Miner.* **2019**,
504            DOI: 10.1007/s00269-019-01028-y

505    (34)    Soltermann, D.; Marques Fernandes, M.; Baeyens, B.; Dähn, R.; Miehé-Brendlé, J.;
506          Wehrli, B.; Bradbury, M. H. Fe(II) Sorption on a Synthetic Montmorillonite. A
507          Combined Macroscopic and Spectroscopic Study. *Environ. Sci. Technol.* **2013**, *47(13)*,
508          6978–6986.

509    (35)    Bunau, O.; Joly, Y. Self-Consistent Aspects of X-Ray Absorption Calculations. *J. Phys.*
510          *Condens. Matter* **2009**, *21(34)*, 345501.

511    (36)    Kéri, A.; Dähn, R.; Krack, M.; Churakov, S. V. Combined XAFS Spectroscopy and *Ab*
512          *Initio* Study on the Characterization of Iron Incorporation by Montmorillonite. *Environ.*
513          *Sci. Technol.* **2017**, *51(18)*, 10585–10594.

514    (37)    Churakov, S. V.; Daehn, R. Zinc Adsorption on Clays Inferred from Atomistic
515          Simulations and EXAFS Spectroscopy. *Environ. Sci. Technol.* **2012**, *46(11)*, 5713–5719.

516    (38)    Churakov, S. V. *Ab Initio* Study of Sorption on Pyrophyllite: Structure and Acidity of
517          the Edge Sites. *J. Phys. Chem. B* **2006**, *110(9)*, 4135–4146.

518    (39)    Sainz-Diaz, C. I.; Palin, E. J.; Hernández-Laguna, A.; Dove, M. T. Octahedral Cation
519          Ordering of Illite and Smectite. Theoretical Exchange Potential Determination and
520          Monte Carlo Simulations. *Phys. Chem. Miner.* **2003**, *30(6)*, 382–392.

521    (40)    Sainz-Díaz, C. I.; Timón, V.; Botella, V.; Artacho, E.; Hernández-Laguna, A. Quantum
522          Mechanical Calculations of Dioctahedral 2:1 Phyllosilicates: Effect of Octahedral Cation
523          Distributions in Pyrophyllite, Illite, and Smectite. *Am. Mineral.* **2002**, *87(7)*, 958–965.

524    (41)    CP2K developers group (2002-2018): www.cp2k.org.

525    (42)    VandeVondele, J.; Krack, M.; Mohamed, F.; Parrinello, M.; Chassaing, T.; Hutter, J.
526          QUICKSTEP: Fast and Accurate Density Functional Calculations Using a Mixed
527          Gaussian and Plane Waves Approach. *Comput. Phys. Commun.* **2005**, *167(2)*, 103–128.

528    (43)    Goedecker, S.; Teter, M.; Hutter, J. Separable Dual-Space Gaussian Pseudopotentials.
529          *Phys. Rev. B* **1996**, *54(3)*, 1703–1710.

530    (44)    Krack, M. Pseudopotentials for H to Kr Optimized for Gradient-Corrected Exchange-
531          Correlation Functionals. *Theor. Chem. Acc.* **2005**, *114(1–3)*, 145–152.

532    (45)    VandeVondele, J.; Hutter, J. Gaussian Basis Sets for Accurate Calculations on Molecular
533          Systems in Gas and Condensed Phases. *J. Chem. Phys.* **2007**, *127(11)*, 114105.

534    (46)    Perdew, J. P.; Burke, K.; Ernzerhof, M. Generalized Gradient Approximation Made
535           Simple. *Phys. Rev. Lett.* **1996**, *77(18)*, 3865–3868.

536    (47)    Rollmann, G.; Rohrbach, A.; Entel, P.; Hafner, J. First-Principles Calculation of the
537           Structure and Magnetic Phases of Hematite. *Phys. Rev. B - Condens. Matter Mater. Phys.*
538           **2004**, *69(16)*, 165107.

539    (48)    Liechtenstein, A. I.; Anisimov, V. I.; Zaanen, J. Density-Functional Theory and Strong
540           Interactions: Orbital Ordering in Mott-Hubbard Insulators. *Phys. Rev. B* **1995**, *52(8)*,
541           5467–5471.

542    (49)    Dudarev, S. L.; Botton, G. A.; Savrasov, S. Y.; Humphreys, C. J.; Sutton, A. P. Electron-
543           Energy-Loss Spectra and the Structural Stability of Nickel Oxide: An LSDA+U Study.
544           *Phys. Rev. B* **1998**, *57(3)*, 1505–1509.

545    (50)    Ankudinov, A. L.; Ravel, B.; Rehr, J. J.; Conradson, S. D. Real-Space Multiple-
546           Scattering Calculation and Interpretation of X-Ray-Absorption near-Edge Structure.
547           *Phys. Rev. B* **1998**, *58(12)*, 7565–7576.

548    (51)    Ankudinov, A. L.; Rehr, J. J. Theory of Solid-State Contributions to the X-Ray Elastic
549           Scattering Amplitude. *Phys. Rev. B* **2000**, *62(4)*, 2437–2445.

550    (52)    Rehr, J. J.; Ankudinov, A.; Ravel, B. *User's Guide, FEFF v.8.40*. Seeattle, USA, **2006**,
551           pp. 66.

552    (53)    Manceau, A.; Chateigner, D.; Gates, W. P. Polarized EXAFS, Distance-Valence Least-
553           Squares Modeling (DVLS), and Quantitative Texture Analysis Approaches to the
554           Structural Refinement of Garfield Nontronite. *Phys. Chem. Miner.* **1998**, *25(5)*, 347–
555           365.

556    (54)    Dähn, R.; Scheidegger, A. M.; Manceau, A.; Schlegel, M. L.; Baeyens, B.; Bradbury, M.
557           H.; Morales, M. Neoformation of Ni Phyllosilicate upon Ni Uptake on Montmorillonite:
558           A Kinetics Study by Powder and Polarized Extended X-Ray Absorption Fine Structure
559           Spectroscopy. *Geochim. Cosmochim. Acta* **2002**, *66(13)*, 2335–2347.

560    (55)    Newville, M. IFEFFIT: Interactive XAFS Analysis and FEFF Fitting. *J. Synchrotron*
561           *Radiat.* **2001**, *8*, 322–324.

562    (56)    Ravel, B.; Newville, M. ATHENA , ARTEMIS , HEPHAESTUS : Data Analysis for X-
563           Ray Absorption Spectroscopy Using IFEFFIT. *J. Synchrotron Radiat.* **2005**, *12(4)*, 537–
564           541.

565    (57)    Dähn, R.; Baeyens, B.; Bradbury, M. H. Investigation of the Different Binding Edge
566              Sites for Zn on Montmorillonite Using P-EXAFS – the Strong/Weak Site Concept in the
567              2SPNE SC/CE Sorption Model. *Geochim. Cosmochim. Acta* **2011**, *75(18)*, 5154–5168.

568    (58)    Vespa, M.; Lanson, M.; Manceau, A. Natural Attenuation of Zinc Pollution in Smelter-
569              Affected Soil. *Environ. Sci. Technol.* **2010**, *44(20)*, 7814–7820.

570    (59)    Kaufhold, S.; Stucki, J. W.; Finck, N.; Steininger, R.; Zimina, A.; Dohrmann, R.; Ufer,
571              K.; Pentrák, M.; Pentráková, L. Tetrahedral Charge and Fe Content in Dioctahedral
572              Smectites. *Clay Miner.* **2017**, *52(1)*, 51–65.